An Overview of the Proprotor Performance Test in the 14- by 22-Foot Subsonic Tunnel

Nikolas S. Zawodny
Senior Research Engineer

Kyle A. Pascioni
Research Aerospace Engineer

Christopher S. Thurman
Research Aerospace Engineer

Hampton, VA, USA
NASA Langley Research Center

ABSTRACT

This work experimentally investigates the aerodynamic behavior of proprotors across a wide range of angles of attack. These flight conditions are intended to be representative of Urban Air Mobility (UAM) vehicle platforms that utilize articulating propulsors to transition from a vertical takeoff and landing (VTOL) phase typical of a conventional rotorcraft to an axial mode of forward flight typical of a fixed-wing aircraft. These data are used to identify the potential limits of lower-fidelity aerodynamic modeling tools, as well as to inform future acoustic phases of testing. Tests were conducted on two proprotor designs in the NASA Langley 14- by 22-Foot Subsonic Tunnel using an articulating propeller test stand. Hover results identified unique flow physics on one of the proprotors, including severe outboard flow separation and perpendicular blade-vortex interactions on the outboard portions of the blades. Transition and forward flight conditions yielded informative trends in terms of both on- and off-axis forces and moments against which low-fidelity prediction models were compared.

NOTATION

c Section blade chord (m)
c' Reference section blade chord at r' (m)
$c_{l,\alpha}$ Section lift slope (1/rad)
C_m $= 4\pi^2 m/(\rho\Omega^2 D^5)$, Pitching moment coefficient
C_T $= 4\pi^2 T/(\rho\Omega^2 D^4)$, Thrust coefficient
C_P $= 8\pi^3 Q/(\rho\Omega^2 D^5)$, Power coefficient
C_N $= 4\pi^2 N/(\rho\Omega^2 D^4)$, Normal force coefficient
C_n $= 4\pi^2 n/(\rho\Omega^2 D^5)$, Yawing moment coefficient
C_Y $= 4\pi^2 Y/(\rho\Omega^2 D^4)$, Side force coefficient
D Proprotor diameter (m)
DL $= T/(\pi R^2)$, Disk loading (N/m^2)
FM $= T^{3/2}/(\Omega Q\sqrt{2\rho\pi R^2})$, Figure of merit
J $= 2\pi V_\infty/(\Omega D) = \pi M_\infty/M_{tip}$, Advance ratio
K_T, K_P Thrust and power coefficient empirical constants
m Pitching moment (Nm)
n Yawing moment (Nm)
N Normal force (N)
N_b Number of proprotor blades
Q Torque (Nm)
r Normalized blade span location relative to R
r' $= 0.75$, Normalized reference blade span location
R Proprotor radius (m)
T Thrust (N)
V_∞ Freestream velocity (m/s)
Y Side force (N)
α_0 Airfoil zero-lift angle of attack (deg.)

α_p Proprotor angle of attack (deg.)
β' $= \Theta_{tw,0.75R} + \theta_0$, blade angle at $0.75R$
η $= C_T J/C_P$ Propulsive efficiency
Ω Rotational speed (rad/s)
ρ Freestream density (kg/m^3)
$\sigma(r)$ $= N_b c(r)/(\pi R)$, Solidity at station r
σ_e Effective solidity
Θ_{tw} Blade twist (deg.)
θ_0 Blade root pitch (deg.)

INTRODUCTION

Propellers have historically been designed and studied with the main intention of thrust generation in axial forward flight. Recently, Advanced Air Mobility (AAM) or Urban Air Mobility (UAM) platforms utilize tilting (articulating) propulsors to deliver vertical lift during takeoff and landing in addition to fulfilling forward thrust requirements in cruise. For instance, Figure 1 is a conceptual tiltwing configuration exemplifying the dual use of its propulsors (Ref. 1). Similarities are found on existing tiltrotor vehicles such as the V-22, although many AAM proprotors (or propellers) lack cyclic pitch control. Complex aerodynamic behavior at the high angles of attack and low advance ratios typical of a transition operational condition increase the difficulty of modeling and prediction. To this end, experimental data are needed to better understand the pitfalls of existing modeling techniques. Thus, the objective of the test documented in this paper was to acquire aerodynamic measurements of transition flight conditions representative of AAM configurations. This is part of a planned two-phase wind tunnel test effort, with this first entry dedicated to proprotor aerodynamic loading measurements. The

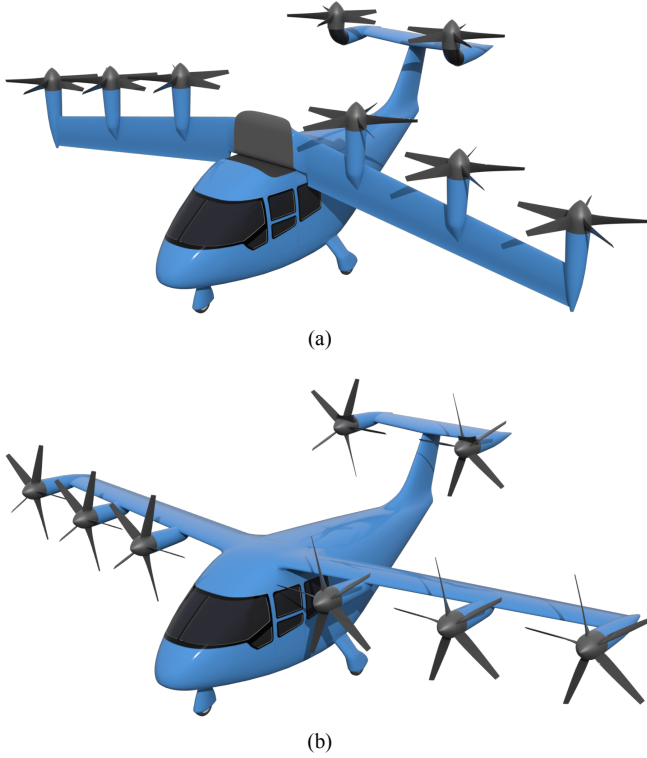second entry will be dedicated to measuring proprotor acoustics.

(a)

(b)

Figure 1: NASA tiltwing concept in (a) VTOL and (b) forward flight modes (Ref. 1).

There is an increasing need for tools to predict propulsor forces and moments for all flight regimes, particularly during a transition between hover and forward flight involving tilting propulsors. The dataset described herein is useful to assess the validity of analytical and numerical models for propulsors at nonzero incidence. A plethora of lower-fidelity aerodynamic models exist, which could be used for initial propulsor sizing or vehicle design optimization. With regard to analytical modeling of forces and moments, those proposed by Leng (Refs. 2, 3) will be used in this work. Specifically, Von Mises' (Ref. 4) linear approximimation is extended to estimate on-axis efforts. The prediction of off-axis forces and moments build upon the pioneering momentum theory method of Ribner (Refs. 5, 6) and high incidence considerations of De Young (Ref. 7). These analytical formulations compare overall favorably to measurements (Ref. 8).

Methods of higher fidelity are also numerous and vary in complexity. Blade element momentum theory (BEMT) is one of the most common and relatively efficient numerical tools that works well under hover and axial flight conditions (Ref. 9). While modifications have been made to extend BEMT to propulsors at incidence, for example, by accounting for nonuniform inflow about the azimuth (Ref. 10), accuracy tends to reduce at the large angles of attack found in transitioning propulsors even when considering stall (Ref. 11). Conversely, blade element theory with dynamic inflow models (Refs. 12–14) often produces accurate aerodynamic predictions for edgewise flight and can even provide off-body flowfield information away from the propulsor disk. Further increasing fidelity, free-wake models solve for the propulsor wake geometry directly and can be used to compute inflow characteristics that enable calculation of forces and moments. The Comprehensive Analytical Model of Rotorcraft Aerodynamics and Dynamics (CAMRAD II) (Ref. 15) has the ability to run free-wake analyses. This code was selected for this work given the option to couple with an appropriate F1A solver for acoustic prediction which will be assessed in the future.

The remainder of this paper begins with an overview of the experiment, specifically, the proprotor designs and wind tunnel facility. Details on the test stand and measurements are also included, along with oil flow visualization as to why one proprotor design will be emphasized in the results section. An overview of the computational methods will then be given. Finally, a comparison of modeled and measured on- and off-axis forces and moments will be provided and discussed.

PROPROTOR DESIGNS

Two proprotor designs were used throughout this work: the first is a five-bladed optimum hovering proprotor, hereby denoted as the OPT5, and the second is a five-bladed computationally optimized proprotor, or the COPR5 (Ref. 16). Photographs of the tested proprotors are provided in Fig. 2. An 'optimum hovering rotor' can be defined as one that has both minimal induced power requirements and minimal profile power requirements (Ref. 9) using BEMT. The minimal induced power comes from a twist distribution,

$$\Theta_{tw}(r) = \frac{1}{r}\left(\frac{4\pi R C_{T_{design}}}{5.73 N_b c(r)} + \sqrt{\frac{C_{T_{design}}}{2}}\right) - \alpha_0, \quad (1)$$

which is designed to produce uniform inflow over the blade span. The minimal profile power comes from a tapered chord distribution,

$$c(r) = \frac{c_{tip}}{r}, \quad (2)$$

which allows for each radial station to operate at an optimal lift-to-drag ratio. In these equations, r is the normalized span location, $C_{T_{design}}$ is the desired thrust coefficient, α_0 is the zero-lift angle of attack of the airfoil, and c_{tip} is the chord length at the blade tip. A taper distribution of this form is typically not physically realizable, so a linear taper distribution is used in practice.

A two-bladed variant of the 'optimum hovering rotor' was evaluated in Refs. 17–19 during anechoic chamber and wind tunnel testing campaigns, and an OPT5 proprotor was also designed with a NACA 0012 airfoil ($\alpha_0 = 0°$) for use on a
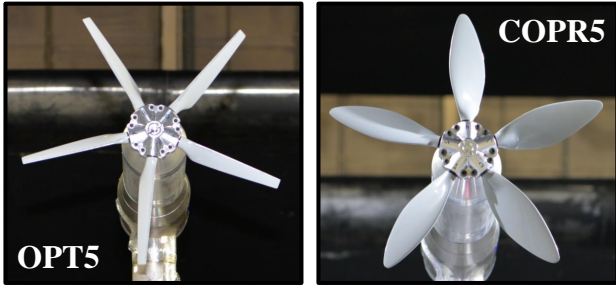
Figure 2: Photographs of the proprotors tested in this study [Source: NASA].

tiltwing vehicle platform in Ref. 1. Since the focus of the wind tunnel testing campaign detailed in this work was proprotor transition regimes, the OPT5 proprotor of Ref. 1 was selected as one of the designs for this work.

The OPT5 proprotor of Ref. 1 was scaled down to model size by a factor of 3.61 while maintaining typical nondimensional quantities such as $C_T/\sigma_{mean} = 0.123$, disk loading, $DL = 960$ N/m^2 (20 lb/ft^2), and $M_{tip} = 0.50$ in the hover operating condition. The scaled geometry had a disk radius of $R = 0.3048$ m (1 ft.), $c_{tip} = 0.025$ m (0.97 in.) and was designed to produce 280 N (62.85 lbs.) of thrust at a target rotation rate of $\Omega = 558$ rad/s (5332 RPM). The resultant twist and taper distributions produced using Eqs. 1 and 2, as well as the linear taper distribution that was used for the OPT5 proprotor, are shown in Fig. 3.

The COPR5 is a proprotor whose blade shape is optimized for minimum noise radiation at a target cruise condition. It was optimized using an adjoint optimization method that employed the CCBlade.jl BEMT code (Ref. 20), using a baseline helically twisted propeller as an initial input geometry. The constraint criteria for the proprotor optimization were generated thrust and radiated tonal noise in the plane of the proprotor, with an objective function that sought to maximize the cruise efficiency. It is worth noting that the original proprotor design was three-bladed (COPR3), and the blade count was increased to five (COPR5) in an effort to assess the additional noise reduction benefits associated with reduced aerodynamic loading per proprotor blade. The twist and chord distributions of the COPR5 blade are also provided in Fig. 3. The target design operating condition of COPR3 is at a rotation rate of Ω = 3640 RPM and a freestream Mach number of M_∞ = 0.111. COPR5 was found in a previous investigation (Ref. 21) to exhibit peak propulsive efficiency at a slightly lower rotation rate of 3400 RPM for the same forward flight condition. Similar to the OPT5, COPR3 and COPR5 nominally maintain a constant NACA 0012 airfoil profile along the entire blade span.
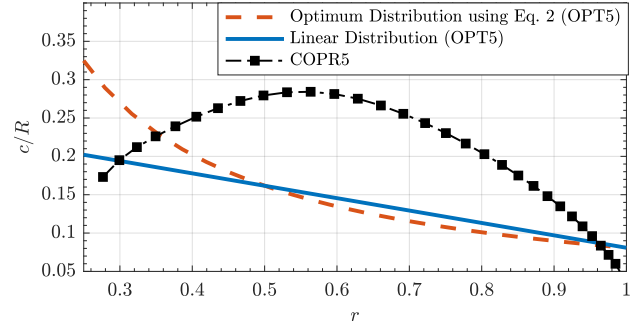
EXPERIMENTAL SETUP AND MEASUREMENT TECHNIQUES

Wind Tunnel Facility

Performance measurements of two different isolated proprotors were acquired in the NASA Langley Research Center 14-
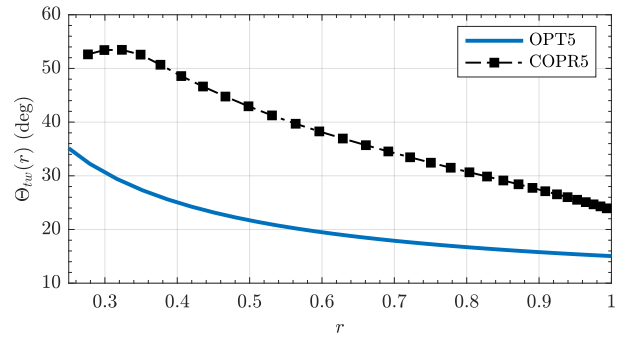
(a)

(b)

Figure 3: OPT5 and COPR5 (a) twist distributions, $\Theta_{tw}(r)$, and (b) chord distributions, $c(r)$.

by 22-Foot Subsonic Tunnel. This facility has been used extensively for both aerodynamic and acoustic studies (Ref. 22). Given the size of the test section, proprotor diameter, and nominal thrust produced by the proprotors, mean facility effects on the proprotor aerodynamics are assumed to be minimal. Two inflow probes were also utilized during the test: a Brüel & Kjær type 4138 microphone outfitted with a conical nosecone and a single-axis hotwire probe powered using a Dantec miniCTA system. These probes were used to provide insight for future acoustic testing and to determine freestream turbulence in the open configuration of the wind tunnel test section, respectively. However, these data are reserved for future publications. A photograph of the propeller test stand and inflow instrumentation installed in the wind tunnel test section is provided in Fig. 4.

Propeller Test Stand

The proprotor test articles were operated using the NASA Langley Propeller Test Stand (PTS). The PTS was designed to evaluate installed propeller/rotor noise and performance in the NASA wind tunnel facilities (Ref. 23). The PTS is equipped with a water-cooled drive motor that is capable of continuous 52 kW operation with an operational speed range of 250 to 16000 RPM. The PTS also has roll, pitch, and yaw capabilities with respective limits of $\pm$ 180°, $\pm$ 25°, and $\pm$ 90° in the wind tunnel reference frame, all with an accuracy of $\pm$ 0.1°. The PTS is outfitted with a six-component multiaxis load cell for

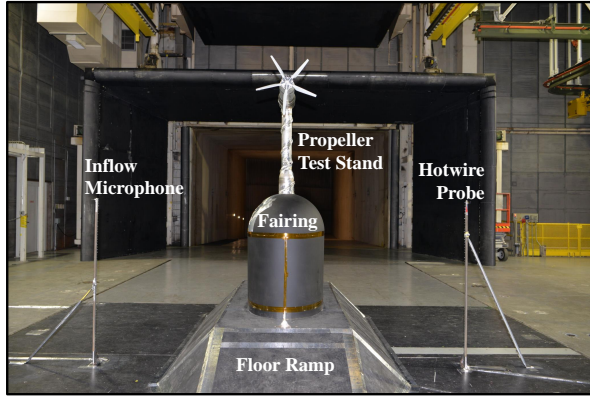Figure 4: Propeller test stand components and inflow measurement probes [Source: NASA].

Figure 5: Cut-away view illustrating the primary components of the PTS motor assembly.

aerodynamic force measurements, an aft-mounted triaxial accelerometer for vibration assessment, a laser sensor tachometer for rotation rate monitoring, and a series of thermal probes for motor health diagnostics. The base of the PTS structure was concealed from the test section flow field by means of an airfoil "tear drop" fairing as well as an elevated floor ramp structure.

Figure 5 provides a cut-away view of the PTS motor assembly. As this image shows, the motor consists of an inrunning rotor and shaft (rotor assembly) that is positioned within the stator assembly. The rotor assembly is axially and radially held in place by means of forward and aft bearings. Water cooling of the stator assembly is performed by means of a brass cooling jacket. The motor stator assembly can be fixtured to the stationary PTS fuselage in two locations: a forward-mounted adapter between the outer fuselage and forward bearing, and the aft-mounted ATI-IA Mini85 multiaxis load cell. The presence of this fuselage/bearing adapter at the front of the stator assembly was previously deemed unsuitable for measuring off-axis loads due to the physical bridging of the load cell with the fuselage. Therefore, this adapter (shaded red in Fig. 5) was removed at the onset of testing. While this did result in a large static cantilever load and moment exerted on the load cell, it was found to remain within loading range for which the load cell was calibrated.

Test Conditions

Experimental aerodynamic conditions are summarized in Table 1 for each proprotor geometry. Conditions span parameter ranges representative of hover, denoted in the table as 'H', transition conditions 'T' with flow at angles of incidence up to $\alpha_p = 52°$ relative to the freestream, and an advance ratio (J) sweep for axial forward flight 'FF'. Figure 6 provides images of the test setup illustrating the range of proprotor orientations tested. Note that the proprotor is yawed in the wind tunnel frame of reference to emulate the proprotor at an angle of attack in actual flight. Figure 7 provides the relation of the measured forces and moments with nomenclature definitions
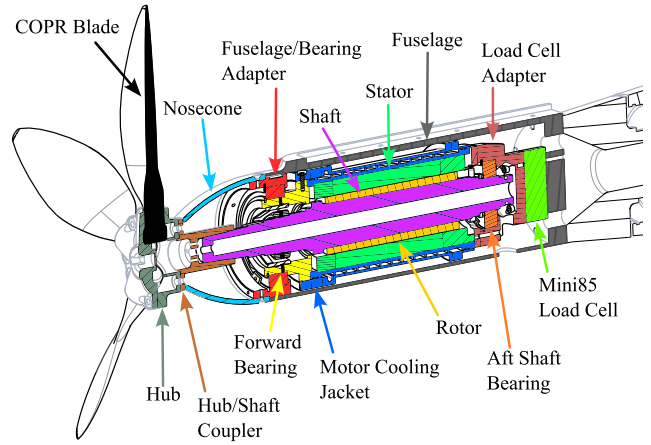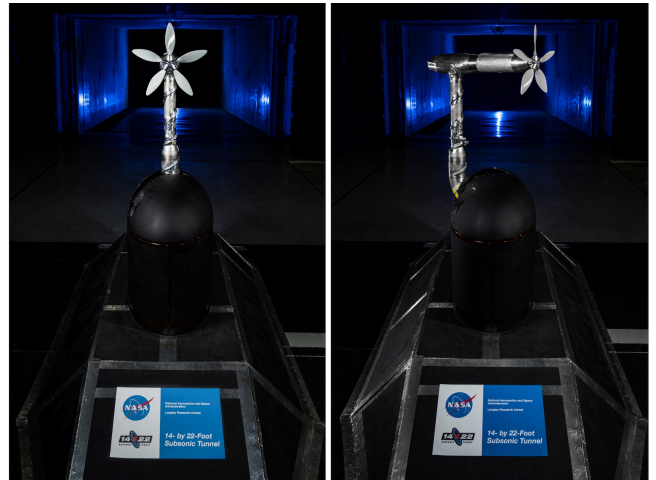

Figure 6: The COPR5 proprotor installed in the Langley 14-by 22-Foot Subsonic Tunnel oriented (*left*) during hover and forward flight conditions ($\alpha_p = 0°$), and (*right*) a transition-like condition in which $\alpha_p = 52°$ [Source: NASA].

corresponding to actual flight. For each of these categories, a subset of the blade root pitch (θ_0) settings were chosen.

Due to the relatively low Reynolds numbers of the tested proprotors, there is speculation as to the applicability of aerodynamic data for a propulsor at this scale to one of a full-sized vehicle. Specifically, the maximum chordwise Reynolds number experienced by the OPT5 rotor encompasses a range of $1.8 \times 10^5 \leq Re_c(0.75R) \leq 3.2 \times 10^5$ over the tested range of tip speed conditions, while the COPR5 encompasses a range of $2.6 \times 10^5 \leq Re_c(0.70R) \leq 6.5 \times 10^5$. These Reynolds numbers fall in the range of laminar-transitional flow regimes according to conventional flat plate aerodynamic theory. Using the previously mentioned scale factor of 3.61 between the current tested proprotors and that designed for the RVLT tiltwing reference vehicle, these Reynolds numbers approach and exceed $Re_c \sim 10^6$, which falls well into the fully turbulent flow regime. Note that the higher range of Reynolds numbers for the COPR5 is attributed to its larger chord distribution relative

4

Table 1: Conditions tested for each proprotor covering hover (H), transition (T), and forward flight (FF).

Proprotor	Condition	θ_0 (deg.)	β' (deg.)	M_{tip}	J	α_p (deg.)
OPT5	H	$0^{\dagger\ddagger}, 8^{\dagger\ddagger}$	17, 25	$0.27 - 0.52$	0	–
	T	$8^{\dagger}, 16^{\dagger}$	25, 33	$0.12 - 0.52$	$0.1 - 1.7$	$5 - 52$
	FF	$8^{\dagger}, 16^{\dagger}, 24^{\dagger}$	25, 33, 41	$0.12 - 0.52$	$0.35 - 1.7$	0
COPR5	H	$-15^{\dagger\S}$	17.5	$0.20 - 0.50$	0	–
	T	$-10^{\S}, -7.5^{\S}, -5^{\S}$	22.5, 25, 27.5	$0.20 - 0.43$	$0.4 - 1.4$	$5 - 50$
	FF	$0^{\S}$	32.5	$0.10 - 0.39$	$0.2 - 1.5$	0

†*No trip.*
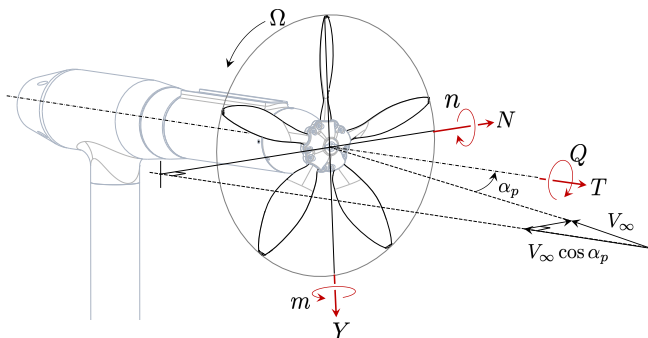‡*Sand grit.*
§*Serrated tape.*

Figure 7: Schematic of the defined proprotor forces and moments.

to the OPT5, which is presented in Fig. 3(b).

To investigate the low Reynolds number behavior of the proprotors, two methods of blade surface tripping were considered: sand grit and serrated tape. A sand grit of characteristic height of 0.010" (0.254 mm) was adhered along the OPT5 blade leading edge on both suction and pressure sides of the blade. The chordwise extent of the grit was approximately up to $0.25c$. A serrated trip tape of 0.005" (0.127 mm) thickness was also tested along the leading edge region of the suction side of the blade and was approximately 0.25" (6.35 mm) long in the chordwise direction. The serrated tape tripping technique was tested for both proprotors, whereas the gritting method was only tested on the OPT5 proprotor. Results will only be shown with serrated tape given its effectiveness relative to sand grit. Surface oil flow visualizations were also performed on the OPT5 and COPR5 blades in hover conditions.

Surface oil flow is an excellent tool for visualizing bulk flow behavior on aerodynamic surfaces, such as flow separation. While several oil types were attempted, the most successful was Aeroshell Aviation Oil 100. Oil flow visualization runs involved application of the oil to a single blade using a foam brush, running the PTS for several minutes at a target rotation rate, then quickly shutting down the PTS to allow quick

observation of the oil-brushed blade using an ultraviolet lamp and high-resolution camera. The OPT5 was operated at $M_{tip} = 0.50$ and $\theta_0 = 0°$ for the oil flow runs since this is the condition for which it was designed to achieve the hover disk loading of the RVLT tiltwing concept (Ref. 1). The COPR5, meanwhile, was operated at $M_{tip} = 0.45$ and $\theta_0 = -15°$ since this condition was able to achieve the same desired disk loading.

Measurement Uncertainty

Previous investigations have revealed that the Mini85 load cell has the potential to exhibit output DC voltage drift when exposed to temperature gradients (Refs. 21, 24). In the context of the current test setup, there are several sources of temperature gradient that can be encountered by the load cell. These include changes in the temperature of the flow over the PTS fuselage, the changing temperature of the motor and aft bearing assembly during operation, and the entrance and exit of the liquid coolant lines that pass through the aft mounting surface of the fuselage. As is shown in Fig. 5, the Mini85 is sandwiched between the aft fuselage surface and the motor aft bearing assembly. To mitigate these thermal drift impacts on the load measurements, a "thermal soaking" procedure was implemented at the onset of every run sequence. This consisted of running the PTS and proprotor assembly at a midrange loading condition for a period of time until the thrust measurement output by the load cell was seen to exhibit steady behavior. This midrange loading condition varied between hover and forward flight conditions, as did the respective settling times for the load cell. On average, however, this thermal soaking took approximately 15-20 minutes of PTS and proprotor operation time in either static tunnel conditions (hover) or at a middle range flow speed condition (forward flight). At the conclusion of this thermal soaking, both the PTS and wind tunnel were brought down to idle conditions and a zero load "tare" condition was taken, after which a run sequence was initiated.

While the thermal soaking method greatly reduced the levels of DC thermal drift in the load cell measurements, slight deviations were encountered throughout the test campaign. Therefore, a constant repeatability error was assumed based on a

series of repeat run conditions performed throughout the different run sequences. The repeatability errors for the hover (H), forward flight (FF), and transition (T) run sequences are provided in Table 2. Figures 8 and 9 display examples of the propagated uncertainties for both on- and off-axis nondimensional force and moment coefficients at transition conditions, which will be emphasized in the results section. Uncertainty bars are plotted for a representative subset of data for clarity. The side force and pitching moment coefficients display similar uncertainty behavior as the normal force and yawing moment coefficients, respectively.

Table 2: Proprotor force and moment repeatability errors for hover and forward flight conditions.

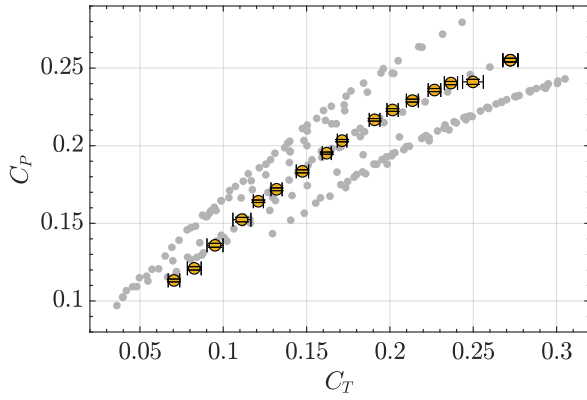| Flight Condition	T, N, Y (N)	Q, n, m (Nm)
H	4.448	0.113
FF, T	2.224	0.057

Figure 8: Measurement uncertainty for thrust and power coefficients for the COPR5 in transition. The full dataset is given by grey markers, and a representative subset is highlighted by yellow markers.
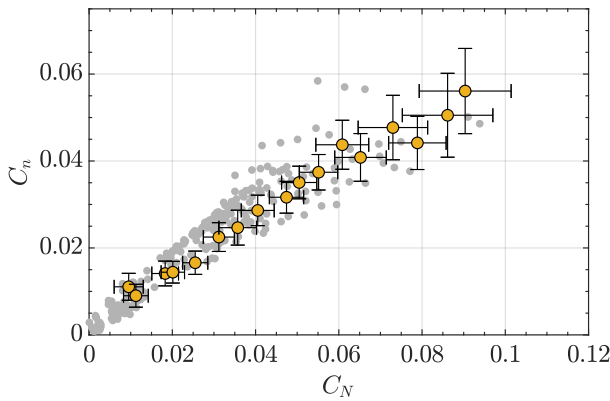

Figure 9: Measurement uncertainty for normal force and yawing moment coefficients for the COPR5 in transition. The full dataset is given by grey markers, and a representative subset is highlighted by yellow markers.

COMPUTATIONAL TOOLS

Analytical and numerical methods of varying fidelity are implemented and compared with the processed aerodynamic performance data of the COPR5. For additional numerical analysis focused on the OPT5 including modifications to the blade geometry to enhance hover performance, the reader is referred to a companion paper in Ref. 25. The assessments herein are aimed at better understanding the valid operating range of select models compared to the experimental data. The analytical modeling described below is for efficient evaluation and may be best suited for initial whole-aircraft design, as results can be obtained on the order of milliseconds. Modeling using CAMRAD II provides computations with much more embedded physics but with higher computational time, e.g., tens to hundreds of seconds depending on the types of submodels chosen.

Analytical Modeling

We seek to estimate the relevant force and moment coefficients as a function of the operating conditions; specifically, the proprotor angle of attack, advance ratio, and blade pitch setting,

$$C_T, C_P, C_N, C_n = f(\alpha_p, J, \beta'). \tag{3}$$

Von Mises (Ref. 4) proposed linear equations for thrust and power coefficients in forward flight. These equations were more recently extended by Leng et al. (Ref. 2) to account for proprotors at incidence, which will be used here. The extension incorporates the average effect of varying blade angle of attack and dynamic pressure over the proprotor azimuth,

$$C_T(\alpha_p, J, \beta') =$$
$$K_T \pi r' \sigma_e \cos \beta' \left[J_{0T} - J \cos \alpha_p + \frac{J_{0T}}{2} \left(\frac{J \sin \alpha_p}{\pi r'} \right)^2 \right], \tag{4}$$

and

$$C_P(\alpha_p, J, \beta') =$$
$$K_P (\pi r')^2 \sigma_e \sin \beta' \left[J_{0P} - J \cos \alpha_p + \frac{J_{0P}}{2} \left(\frac{J \sin \alpha_p}{\pi r'} \right)^2 \right]. \tag{5}$$

Here, K_T and K_P are constants used to fit to the measurements and are chosen to be 0.80 and 0.67, respectively, and $r' = 0.75$ is the reference normalized blade span location. Similar to De Young (Ref. 7) and Alba (Ref. 26), the effective solidity is defined as

$$\sigma_e = \frac{4N_b}{3\pi} \frac{\bar{c}}{D} \frac{\bar{c}_{l,\alpha}}{0.95(2\pi)}, \tag{6}$$

in which N_b is the number of blades, and $\bar{c}$ and $\bar{c}_{l,\alpha}$ are the average blade chord and average airfoil lift curve slope from $0.2R$ to R, respectively. Note that the lift curve slope is used to scale the typical lift curve slope value of $0.95(2\pi)$. Given the NACA0012 profile of the COPR5 blades, $\bar{c}_{l,\alpha}/(0.95(2\pi)) = 1$. The advance ratio corresponding to that of zero thrust for any given blade pitch setting is

$$J_{0T} = 2.2 \tan(\beta' + 5°). \tag{7}$$

The advance ratio corresponding to that of zero power is

$$J_{0P} = J_{0T} + \frac{16}{\sin\beta'\cos^4\beta'}\left(\frac{\sigma_e}{N_b}\right)^2. \qquad (8)$$

These are given by De Young (Ref. 7), and were derived by fitting experimental data (Ref. 8) from several propellers of varying geometry and blade count. The resulting values agree well with extrapolation of the current dataset, which is also a reasonable approach to determine these parameters.

The normal force and yawing moment coefficients are also given by Ref. 2,

$$C_N(\alpha_p, J, \beta') = \left.\frac{\partial C_N}{\partial \alpha_p}\right|_{\alpha_p=0,J} \frac{2J_{0P} - J\cos\alpha_p}{2J_{0P} - J}\sin\alpha_p, \qquad (9)$$

$$C_n(\alpha_p, J, \beta') = \left.\frac{\partial C_n}{\partial \alpha_p}\right|_{\alpha_p=0,J} \frac{2J_{0T} - J\cos\alpha_p}{2J_{0T} - J}\sin\alpha_p, \qquad (10)$$

respectively. The partial derivatives depend on blade geometry, specifically blade chord and twist distribution, and inflow and dynamic pressure factors formulated from momentum theory. The full set of equations defining these derivatives is given in the Appendix and follow the work of Refs. 2 and 5. These slopes have been previously shown to be accurate only for low to moderate angles of attack (Ref. 27). The remaining terms of Equations 9 and 10 account for the changes in local dynamic pressure and flow angle about the proprotor azimuth enabling a better indication of high-incidence behavior.

CAMRAD II Modeling

A mid-fidelity numerical tool is also selected for this work, namely, CAMRAD II (Ref. 15). This tool is a comprehensive rotorcraft analysis code that allows for the use of different wake models (e.g., uniform inflow, prescribed wake, and free wake) and different blade dynamics (e.g., rigid and elastic). CAMRAD II requires airfoil aerodynamic coefficient data, which can either be generated using analytical equations or can be supplied by the user in the form of an airfoil table. CAMRAD II was used in this work with a single-peak, general free wake geometry model consisting of a second-order trapezoidal distortion integration, a second-order lifting-line with a quarter-chord collocation point, and a wake extent of four revolutions. Since a symmetric NACA 0012 airfoil profile was used for both blade designs, a preexisting airfoil table in the C81 format was used throughout this work. The table was developed using experimental aerodynamic results over $-180° \leq \alpha \leq 180°$ and $0 \leq M_\infty \leq 1$ with a reference Reynolds number of 5.2×10^6 at $M_\infty = 1$. The C81 table data were used by CAMRAD II for predicting spanwise aerodynamic forces and moments. These loads were then integrated over the entirety of the proprotor to produce aerodynamic forces and moments and their respective nondimensional forms.

RESULTS

Hover

Figure 10 provides the figure of merit hover aerodynamic performance profiles of the OPT5 and COPR5 proprotors as a function of tip Mach number. Note that due to the vastly dif-
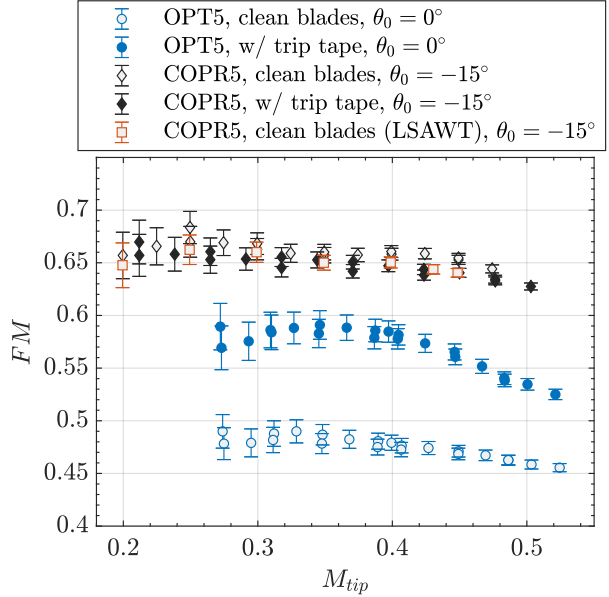

Figure 10: Figure of merit for tested proprotors in hover with clean and trip-taped blades.

ferent solidities of the two proprotors, the objective of this data plot is not to compare their performance to each other, but rather to identify relative changes in performance as a result of blade surface tripping. At the target design operating condition of $M_{tip} = 0.50$, the OPT5 proprotor is seen to have a figure of merit of approximately 0.45, which is dramatically less than the 0.76 predicted by CAMRAD II (Ref. 25). Tripping of the blades was found to increase the figure of merit at this operating condition by nearly 20%. Conversely, COPR5 was found to exhibit practically no variation in performance with surface tripping. Furthermore, excellent performance agreement for the clean COPR5 blades is seen between data from the current test campaign and those measured in the NASA Langley Low Speed Aeroacoustic Wind Tunnel (LSAWT) (Ref. 21).

To gain some additional insight into the flow physics responsible for the hover performance differences between OPT5 and COPR5, Fig. 11 provides surface oil flow visualization of one blade of each proprotor in hover. Due to the fact that the oil is applied to a rotating system, it is important to note that vectors in the illustrations do not represent flow field vectors. Rather, they are the direction taken by the oil flow. Comparing those directions with the lines denoting the centrifugal force direction enables us to infer attached or separated flow. In addition,
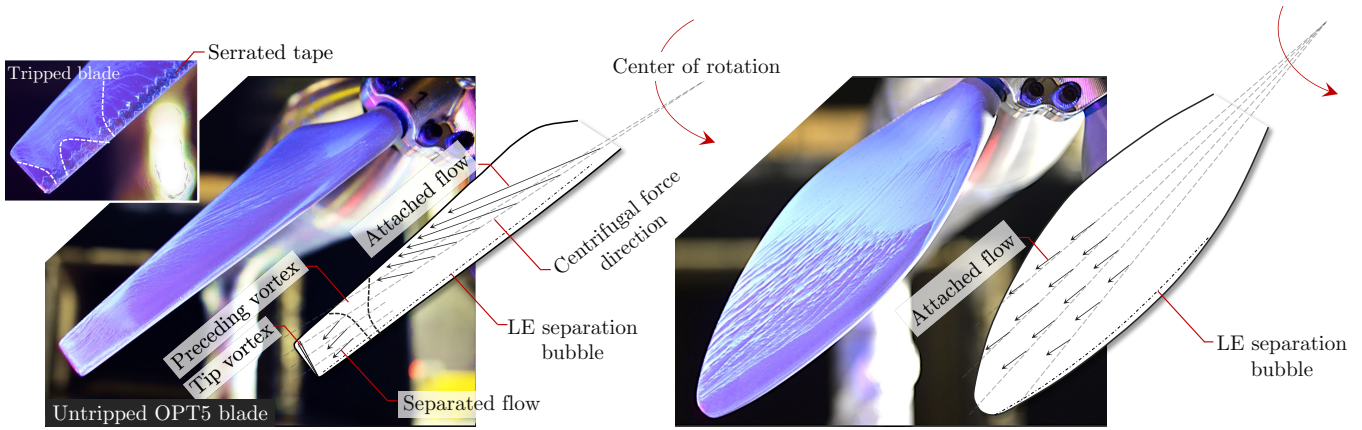
Figure 11: Oil flow visualization using Aeroshell Aviation Oil 100 in hover conditions. The OPT5 (left) was tested at $M_{tip} = 0.50$ and $\theta_0 = 0°$, and COPR5 at $M_{tip} = 0.45$ and $\theta_0 = -15°$ [Source: NASA].

the absence of oil from portions of the blade is also representative of attached flow, since it denotes overcoming of the centrifugal force by the shear force of air over the blade in the chordwise direction.

If attention is focused on the untripped OPT5 blade (left image), a large portion of the outer span of the blade is seen to suffer from flow separation, which is evidenced by the change in direction of the oil streaks from pointing downstream of the centrifugal force direction (further inboard) to pointing upstream. Furthermore, an additional feature can be seen at approximately $0.88R$, which is believed to be representative of the impingement of the tip vortex from the previous blade. Looking at the simulations from Ref. 25, an excerpt of which is given in Figure 12, the simulated skin friction contours provide evidence that the flow is attached on the inboard region of the OPT5, but separated outboard past approximately $0.88R$. While high-fidelity simulations were not run for the COPR5,
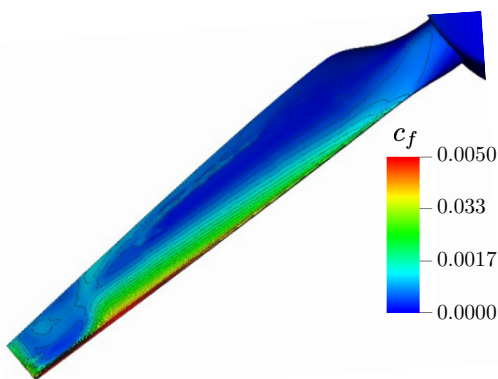

Figure 12: CFD skin friction coefficient of the OPT5 at the same condition as Figure 11 (Ref. 25).

the oil flow results (right) of Fig. 11 indicate attached flow over most of blade span except perhaps close to the root. It is worth noting that the OPT5 design is intended to yield a nearly constant angle of attack along the blade span using BEMT,

whereas COPR5 yields a roll-off in angle of attack along the blade to near zero at the tip region. This roll-off in angle of attack on the COPR5 blade results in very low thrust generation near the tip region of the blade, which likely results in the generation of a tip vortex of low energy. This finding could indicate that shifting of maximum thrust generation further inboard may be a better strategy for UAM vehicle concepts that have high thrust demands for VTOL phases of flight.

Forward Flight

Forward flight performance of the OPT5 and COPR5 was assessed by conducting an advance ratio sweep on the two proprotors by varying their rotation rates and tunnel freestream velocity conditions (see Table 1). Figure 13 provides a profile of propulsive efficiency for the two proprotors. As indicated in Table 1, several collective settings were run for the OPT5 in forward flight, two of which are provided in this plot. The data show that the primary setting of initial focus, $\theta_0 = 24°$, yielded overall very low propulsive efficiency levels. This was found to be due to this collective setting being too aggressive and yielding rather high angles of attack on the outboard part of the OPT5 blades. This is most likely leading to separation and stall on the blades. Reducing the collective to $\theta_0 = 16°$ is seen to greatly improve the propulsive efficiency, the overall trend of which shifts to lower advance ratios.

The propulsive efficiency profile for the COPR5 in Fig. 13 is seen to be very well defined, with a peak of $\eta \approx 0.7$ at an advance ratio of $J \approx 1.1$. Also included in this plot are data from a previous entry in the LSAWT facility (Ref. 21). Both sets of data compare very well with each other, despite the different blade trip conditions between them. This commonality in propulsive efficiency of the COPR5 for different tripping conditions is similar to that observed for hover conditions in Fig. 10. This could be due to the tape height being insufficient relative to the chord length to effectively trip the boundary layer, or the fact that the angles of attack on the blade are modest enough such that a boundary layer trip did
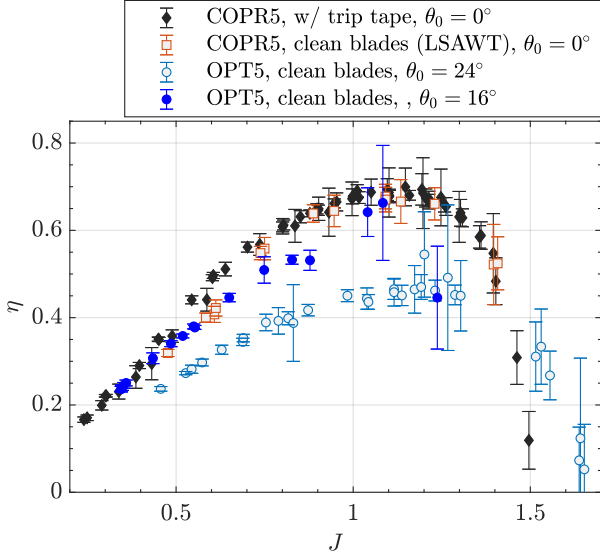
Figure 13: Propulsive efficiency at select conditions for both proprotors in axial forward flight.
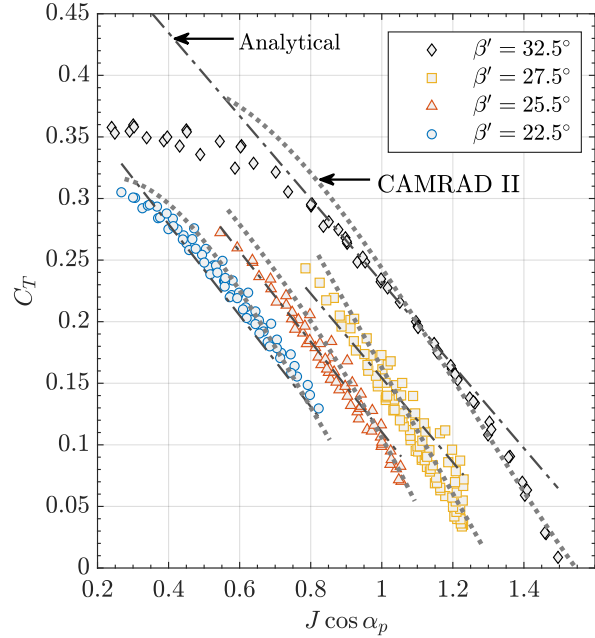

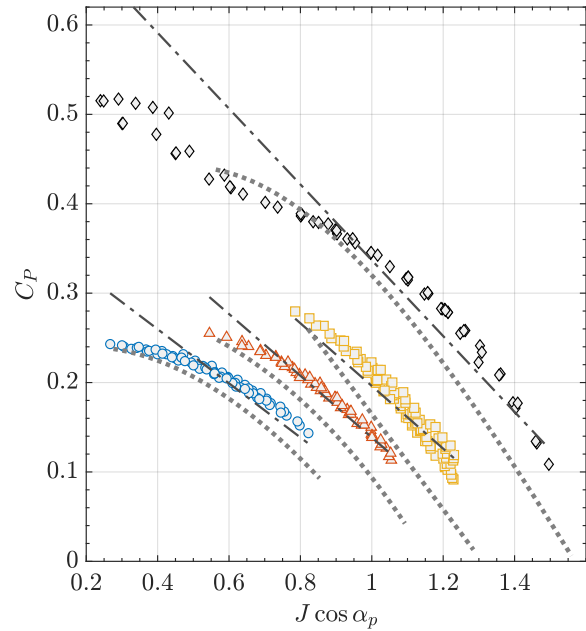Figure 14: Comparison of thrust coefficient between measurements (markers), the analytical prediction, and CAMRAD II.

Figure 15: Comparison of power coefficient between measurements (markers), the analytical prediction, and CAMRAD II.

not have much effect. It is worth noting, however, that there is a slight divergence between the two data sets at advance ratios of $J \leq 0.6$. It is possible that the boundary layer trip could be extending separation and stall effects out to higher angles of attack, thus improving the propulsive efficiency relative to the clean blades for these flight conditions.

Because of the increased knowledge of and confidence in the forward flight performance of the COPR5, it was selected for further investigation of flight transition effects on the proprotor aerodynamics.

Transition

As previously mentioned, the discussion will be limited to COPR5 given the complex aerodynamic phenomena found in the OPT5 data. For the COPR5, thrust and power coefficients over the four different blade pitch settings are given in Figs. 14 and 15. Henceforth, the blade pitch setting will be indicated by the local blade angle at 0.75R, β', rather than the blade root pitch setting, θ_0, given the dependency of the analytical model on β'. As a reminder, these settings and how they are related are summarized in Table 1. The data denoted by $\beta' = 32.5°$ is the forward flight case in which $\alpha_p = 0°$. The remaining data spanning the other three blade angles tested were at nonzero incidence up to $\alpha_p = 50°$. For each blade angle setting, a reasonable trend in the measurements is observed with axial advance ratio. The linear portions of the trends are well captured by the analytical model over the parameterized experimental data spanning advance ratio, proprotor angle of attack, and blade pitch setting. Note that the constants K_T and

9

K_P in equations 4 and 5 are the only 'tuning' parameters to fit the model, specifically, enabling slight adjustments in the slope of the lines. Using a single-value constant for both thrust and power coefficient would result in a reduction in accuracy and is why individual constants were used to provide a best fit for each parameter.

The thrust and power coefficients predicted from CAMRAD II also yield reasonable agreement across the conditions tested. Similar to the analytical model, CAMRAD II captured the individual trends per blade setting. The largest differences with the experiment are between the power coefficients. This is a similar difference found with the analytical model if only a single constant was used between C_T and C_P, e.g., if $K_T = K_P$. For the forward flight condition, advance ratios less than approximately 0.6 produced unreliable CAMRAD II predictions and are omitted from the plot. Upon closer inspection, the blade angles of attack increase with decreasing advance ratio beyond the stall angle, which is approximately 9° for the Reynolds numbers encountered. For example, Figure 16 displays the blade angles of attack in forward flight at the 0.8R span location predicted by CAMRAD II. Adjustments may be
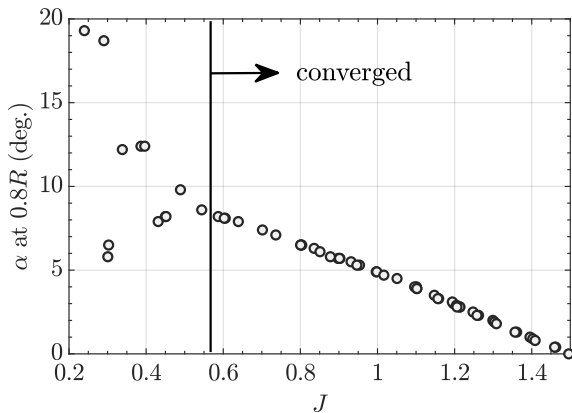

Figure 16: Predicted blade angle of attack at 0.8R for the COPR5 blade in forward flight using CAMRAD II.

made in the future to CAMRAD II to resolve this low advance ratio range. For example, increasing the wake resolution or the number of computed revolutions may prove beneficial.

The off-axis loads arise in transition conditions and are important to characterize as they may affect structural design, stability and control, and aerodynamic interaction with the airframe or other propulsors. Figure 17 summarizes the normal force and yawing moment coefficients computed from the measurements. For each blade pitch setting, the normal force coefficient (corresponding to a vertical force in actual flight) tends to peak at the highest proprotor angles of attack combined with the highest axial advance ratio. As expected, the normal force coefficient increases with proprotor angle of attack for a given axial advance ratio. Similar trends are found for the yawing moment coefficient, which indicates a moment is being generated about the normal force axis influencing the proprotor

to rotate from the starboard to port side of the vehicle in actual flight. This is the result of the difference in higher blade loading on the downgoing blade relative to the lower blade loading on the upgoing blade. Often times this moment is counteracted by another propulsor with opposite rotation direction, but individual propulsor pylons must be able to overcome this aerodynamically-generated moment. For both the normal force and yawing moment coefficients, the trends are quasilinear over the tested proprotor angles of attack. However, it should be noted that Ref. 8 found rapid changes in slope with propeller angle of attack occurring at approximately the cutoff of our test ($\alpha_p = 50°$), with that break in linearity found at progressively lower values of α_p as the axial advance ratio is increased.

Results from the analytical model are also given in Figure 17. For the most part, trends are well captured relative to the measurements. To get a better indication of agreement within the tested conditions, Figure 18 displays the absolute differences in measured versus analytically predicted coefficients. Clearly, the prediction accurately captures the full set of conditions at moderate proprotor angles of attack but diverges at high proprotor angles of attack. For the normal force coefficient, the difference is largest at the combination of high axial advance ratio and proprotor angle of attack. The yawing moment coefficient displays similar disagreement at those conditions but extending over all advance ratios. These differences are similar to those shown in Ref. 2 who also found worsening agreement at proprotor angles of attack beyond those tested here.

With the proprotor orientation as described, the side force and pitching moment are expected to be of secondary importance (Refs. 8, 28). For completeness, however, they are provided in Figure 19. Comparing values with Figure 17, the side force coefficient is indeed smaller than the normal force coefficient, and on average, is approximately 50% less. A similar ratio is found between pitching moment and yawing moment. While it can be argued side force and pitching moment are of secondary importance, clearly these are nonnegligible quantities relative to the previously discussed coefficients. Physically, there is likely an unsteady lift effect in that the peak blade loading occurs azimuthally aft of the peak in blade angle of attack. This misalignment generates force and moment components in the lateral direction in addition to the vertical direction (Ref. 7). In other words, the harmonic blade loading is slightly out of phase with blade angle of attack. When thought of in this light, the side force is equal to the product of the normal force and the sine of this phase angle offset. Similar reasoning can be given for pitching moment and explains the negative sign with respect to its definition in Figure 7. If the angle of attack and blade loading variations are azimuthally aligned and peaking 90 degrees away from the normal force axis, the normal force and yawing moment would increase and the side force and pitching moment would disappear.
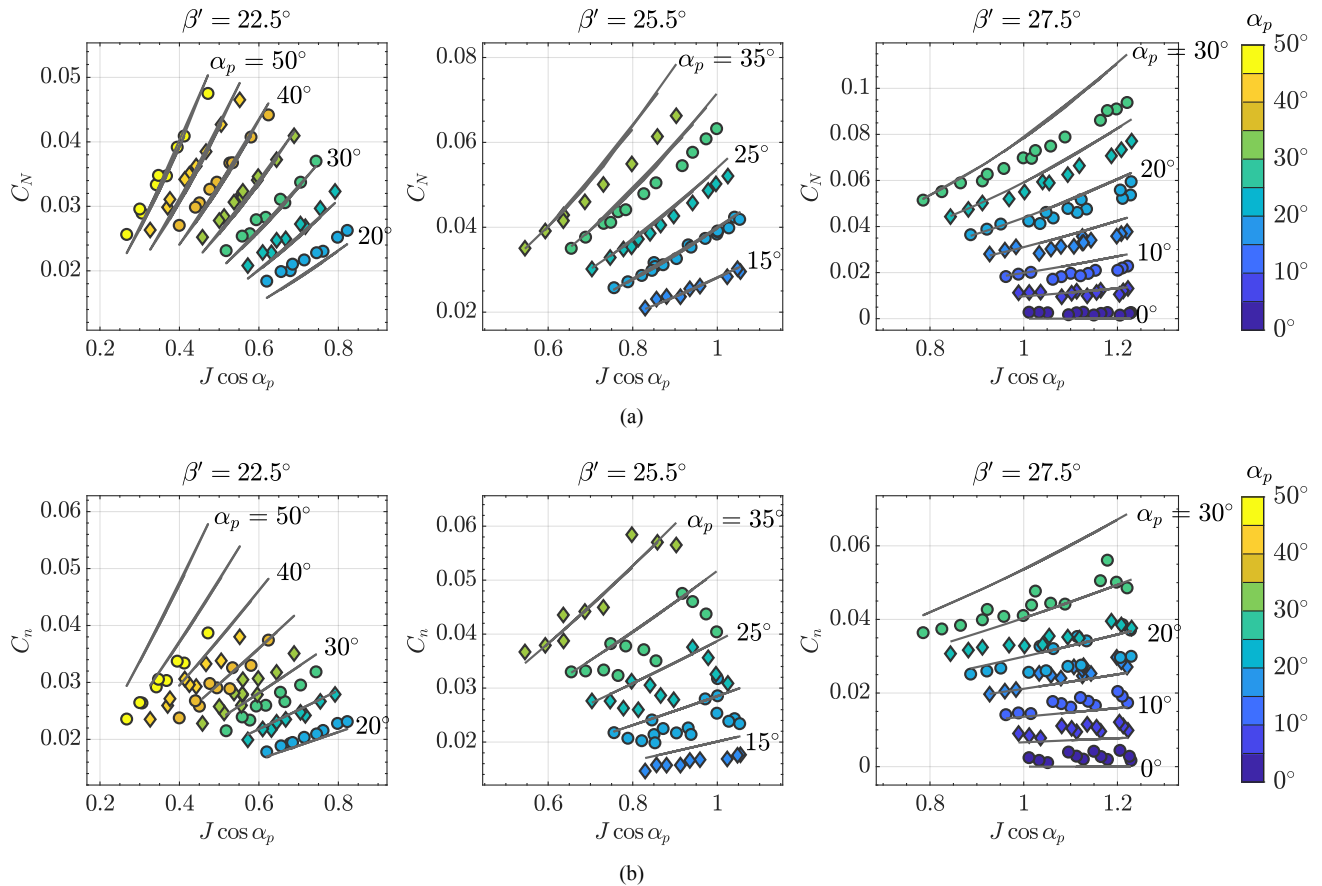
Figure 17: Comparison between measurements (markers) and analytical prediction (lines) of (a) normal force and (b) yawing moment coefficients for the COPR5. Diamond and circle markers denote angles of attack in odd and even multiples of 5, respectively.

CONCLUDING REMARKS

This work investigated the aerodynamic performance of two proprotors across a range of forward flight advance ratios and incidence angles representative of vectored-thrust UAM vehicle configurations. One of these proprotors is a 5-bladed optimum hovering rotor (OPT5), the design of which is determined using traditional rotor BEMT. The second proprotor is also 5-bladed and is the result of a previous acoustic optimization effort (COPR5). The proprotors were analyzed using an articulating propeller test stand outfit with a multiaxis load cell, which allowed for the measurement of the generated on- and off-axis forces and moments. Operating conditions that were analyzed include hovering, VTOL to axial cruise transition, and forward flight conditions.

Hover testing of the proprotors yielded interesting and unexpected flow behavior on the OPT5, which was interrogated in more detail via the use of surface oil flow visualization. The proprotor was found to suffer from severe flow separation on the outer 12% of the blade span, believed to be at least partially due to the interaction of the blade with the tip vortex shed from

the preceding blade. Surface oil flow results of the COPR5, however, were found to show attached flow over the full blade span except perhaps close to the root. This was an interesting discovery since the OPT5 is designed specifically for a hover/VTOL flight condition, whereas COPR5 was designed for forward flight. Simple low-fidelity BEMT tools show that the angles of attack along the COPR5 blade in hover roll off to near zero at the tip, whereas those for OPT5 are theoretically constant along the span. As a result, the peak thrust generation on the COPR5 blades occurs approximately midspan along the blade, while the OPT5 is designed to generate comparable thrust levels along the entire blade span. This could imply that proprotors generating more thrust on the inboard portions of the blade may perform better than conventional rotors for UAM vehicles with high VTOL thrust requirements.

Forward flight conditions yielded clear and identifiable trends in propulsive efficiency as a function of advance ratio for the COPR5. The OPT5, however, suffered from separation and stall effects due to an aggressive collective setting. While limited data were acquired on the OPT5 at a lower collective
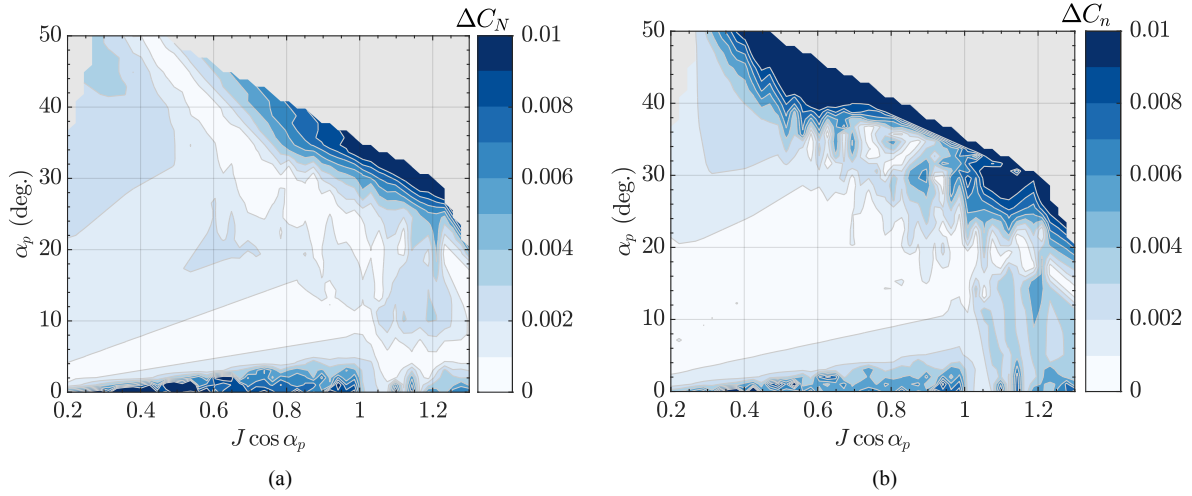
Figure 18: Absolute value of the difference between analytical prediction and measurements of (a) normal force coefficient and (b) yawing moment coefficients for the COPR5.
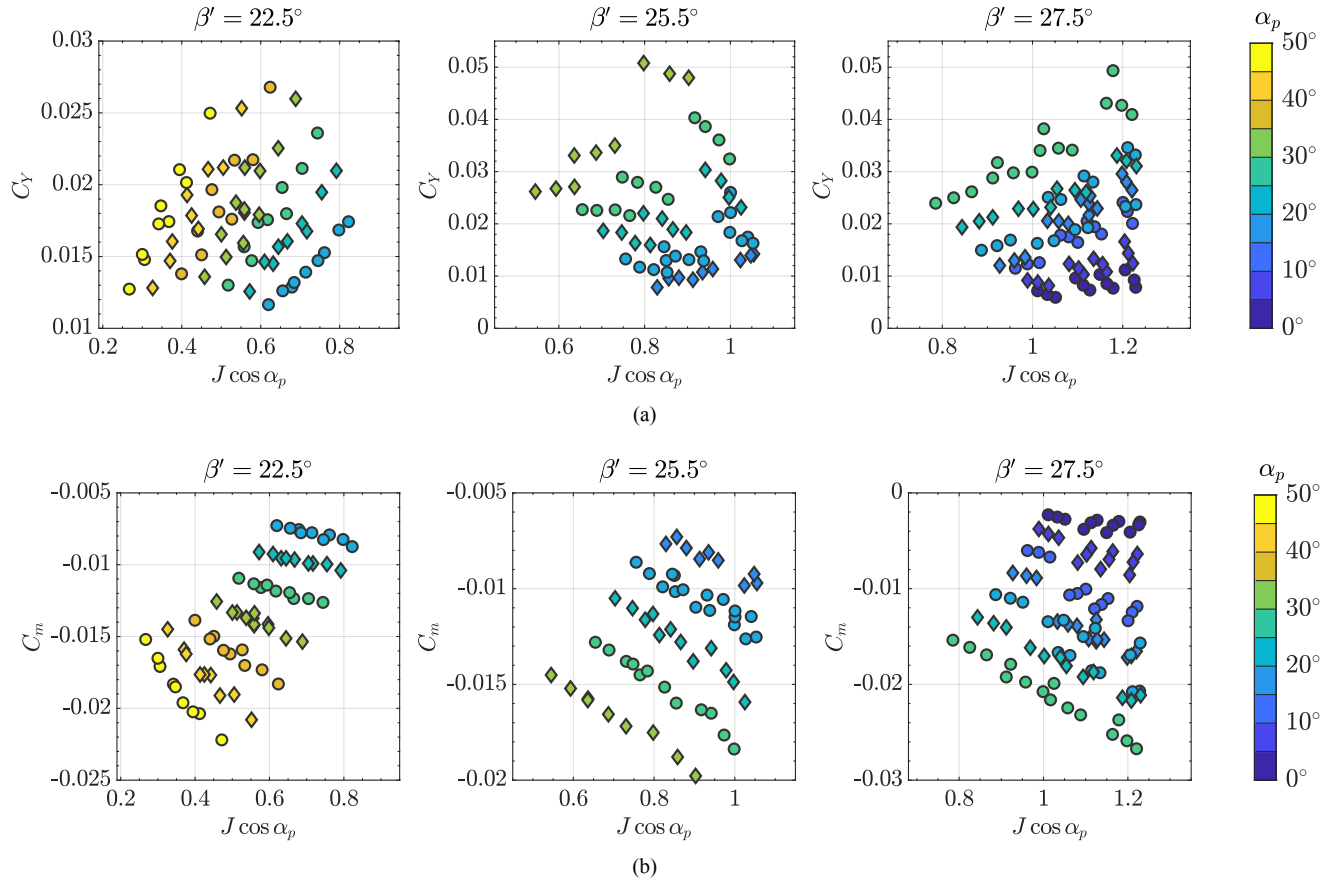

Figure 19: Measured (a) side force and (b) pitching moment coefficient for the COPR5. Diamond and circle markers denote angles of attack in multiples of 5 and 10, respectively.

setting, they are seen to show propulsive efficiencies that are comparable to those of the COPR5.

Transition conditions were investigated up to a maximum proprotor angle of attack $\alpha_p = 52°$. Comparisons of measured on- and off-axis forces and moments including thrust, torque/power, normal force, and yawing moments with theoretical predictions yielding good trend agreements, particularly at higher axial advance ratios and modest angles of attack. While theoretical predictions are currently not available for the side force and pitching moment components, the experimental data are seen to align well with the normal force and yawing moment trends. It is expected that these experimental trends will diverge considerably from analytical predictions at higher proprotor angles of attack, which are very important for vehicles with articulating propulsors.

Future experimental investigations are planned, both into the measurement of proprotor aerodynamic behaviors at incidence angles of $\alpha_p > 52°$, as well as into the acoustics associated with the entire range of transition from VTOL to axial forward flight conditions.

ACKNOWLEDGMENTS

APPENDIX

The partial derivatives used in the analytical model (equations 9 and 10) for normal force and yawing moment are given by Refs. 5 and 2,

$$\left.\frac{\partial C_N}{\partial \alpha_p}\right|_{\alpha_p=0,J} = \frac{\pi}{8} \frac{k_s f(a_i)\sigma_e I_1}{I_1/(I_1-\Delta)+k_a\sigma_e I_1}, \qquad (11)$$

$$\left.\frac{\partial C_n}{\partial \alpha_p}\right|_{\alpha_p=0,J} = \frac{\pi}{8}\left(\frac{k_s f(a_i)}{1+k_a\sigma_e(I_1-\Delta)}\right)\left(\frac{\sigma_e I_2 + 4a_i/\pi}{2(1+\sigma_e I_3)}\right), \quad (12)$$

respectively, in which $k_s = 1.05$ and $k_a = 0.4$ are spinner and sidewash factors and are close to the typical values. Note that a derivation and more thorough approach to setting these values are given in Ref. 5. The dynamic pressure factor,

$$f(a_i) = \frac{J(J+a_i)\left[J(J+a_i)+(J+2a_i)^2\right]}{J^2+(J+2a_i)^2}, \qquad (13)$$

is dependent on advance ratio and the inflow factor given in the equation below. This expression above is a slightly modified version as compared to Ref. 2. This modification was arrived at through inspection and gives resulting partial derivatives within 4% of the original formulation by Ref. 5 over all conditions covered in this paper.

$$a_i = \frac{J}{2}\left[\left(1+\frac{8C_T}{\pi J^2}\right)^{1/2}-1\right]. \qquad (14)$$

The thrust coefficient is taken from Equation 4, although relying on measured thrust would also be acceptable. Three geometric integrals are also used and depend on the ratio between the blade chord distribution and the chord at c' at the reference location $r' = 0.75$, and blade angle distribution, β,

$$I_1 = \frac{3}{4}c_{l,\alpha}\int_{r_0}^{1}\frac{c}{c'}\sin(\beta)\mathrm{d}r, \qquad (15)$$

$$I_2 = \frac{3}{4}c_{l,\alpha}\int_{r_0}^{1}\frac{c}{c'}\cos(\beta)r\mathrm{d}r, \qquad (16)$$

and

$$I_3 = \frac{3}{4}c_{l,\alpha}\int_{r_0}^{1}\frac{c}{c'}\frac{\cos^2\phi}{\sin\phi}r^2\mathrm{d}r, \qquad (17)$$

in which the effective helix angle is estimated as

$$\phi = \tan^{-1}\left(\frac{1+a_i}{1+2a_i}\right). \qquad (18)$$

Finally,

$$\Delta = \frac{(\sigma_e I_2 - 2a_i/\pi)(\sigma_e I_2 + 4a_i/\pi)}{\sigma_e(1+\sigma_e I_3)}. \qquad (19)$$

REFERENCES

1. Whiteside, S., Pollard, B., Antcliff, K., Zawodny, N., Fei, X., Silva, C., and Medina, G., "Design of a Tiltwing Concept Vehicle for Urban Air Mobility," NASA TM 20210017971, 2021.

2. Leng, Y., Moschetta, J.-M., Jardin, T., and Bronz, M., "An Analytical Model for Propeller Aerodynamic Efforts at High Incidence," *54th 3AF International Conference on Applied Aerodynamics*, Paris, France, March 2019.

3. Leng, Y., Jardin, T., Moschetta, J.-M., and Bronz, M., "Analytic Model of Proprotor Forces and Moments at High Incidence," *Journal of the American Helicopter Society*, Vol. 66, (4), 2021, pp. 1–15.

4. Von Mises, R., *Theory of flight*, Courier Corporation, 1959.

5. Ribner, H. S., "Propellers in Yaw," NACA ARR-3L09, 1943.

6. Ribner, H. S., "Propellers in Yaw," NACA Report No. 820, 1945.

7. De Young, J., "Propeller at High Incidence," *Journal of Aircraft*, Vol. 2, (3), 1965, pp. 241–250.

8. Yaggy, P., and Rogallo, V., "A Wind-Tunnel Investigation of Three Propellers through an Angle-of-Attack Range from 0° to 85°," NASA TN D-318, 1960.

9. Leishman, J. G., *Principles of Helicopter Aerodynamics*, Cambridge University Press, New York, NY, 2000.

10. Smith, H., *Engineering models of aircraft propellers at incidence*, Ph.D. thesis, University of Glasgow, 2015.

11. Snel, H., Houwink, R., and Bosschers, J., "Sectional prediction of lift coefficients on rotating wind turbine blades in stall," Technical Report ECN-C-93-052, Netherlands Energy Research Foundation, 1994.

12. Peters, D., Boyd, D., and He, C., "Finite-State Induced-Flow Model for Rotors in Hover and Forward Flight," *Journal of the American Helicopter Society*, Vol. 34, (4), 1989, pp. 5–17.

13. Huang, J., Peters, D., and Prasad, J., "Converged Velocity Field for Rotors by a Blended Potential Flow Method," *GSTF Journal on Aviation Technology (JAT)*, Vol. 1, (2), 2015.

14. Guner, F., Prasad, J., and Peters, D., "An Approximate Finite State Dynamic Wake Model for Predictions of Inflow below the Rotor," *Journal of the American Helicopter Society*, Vol. 66, (3), 2021, pp. 1–10.

15. Johnson, W., *CAMRAD II: Comprehensive Analytical Model of Rotorcraft Aerodynamics and Dynamics, Vols. I – VII*, Johnson Aeronautics, 2020.

16. Ingraham, D., Gray, J. and Lopes, L., "Gradient-Based Propeller Optimization with Acoustic Constraints," AIAA Scitech 2019 Forum, AIAA Paper 2019-1219, San Diego, CA, January 2019.

17. Thurman, C. S., Zawodny, N. S., and Pettingill, N. A., "The Effect of Boundary Layer Character on Stochastic Rotor Blade Vortex Shedding Noise," VFS International 78th Annual Forum & Technology Display, Fort Worth, TX, May 2022.

18. Pettingill, N., Zawodny, N., and Thurman, C., "Aeroacoustic Testing of UAS-Scale Rotors for a Quadcopter in Hover and Forward Flight," 28th AIAA/CEAS Aeroacoustics 2022 Conference, AIAA Paper 2022-3110, Southampton, UK, June 2022.

19. Zawodny, N. S., Pettingill, N. A., and Thurman, C. S., "Identification and Reduction of Interactional Noise of a Quadcopter in Hover and Forward Flight Conditions," Internoise 2022, Glasgow, Scotland, August 2022.

20. Ning, A., "Using Blade Element Momentum Methods with Gradient-Based Design Optimizations," *Structural and Multidisciplinary Optimization*, Vol. **64**, 991–1014 (2021).

21. Zawodny, N. S., Pettingill, N. A., Lopes, L. V., and Ingraham, D. J., "Experimental Validation of an Acoustically and Aerodynamically Optimized UAM Proprotor - Part 1: Test Setup and Results," NASA TM 20220015637, NASA Langley Research Center, 2023.

22. Gentry Jr, G., Quinto, P., Gatlin, G., and Applin, Z., "The Langley 14- by 22-Foot Subsonic Tunnel: Description, Flow Characteristics, and Guide for Users," NASA TP 3008, 1990.

23. Litherland, B., Borer, N., and Zawodny, N., "X-57 Maxwell High-Lift Propeller Testing and Model Development," AIAA AVIATION 2021 FORUM, AIAA Paper 2021-3193, Virtual Event, August 2021.

24. Zawodny, N. S., "Capabilities and Preliminary Checkout of a New Propeller Test Stand," NASA Acoustics Technical Working Group, Virtual Event, April, 2021.

25. Thurman, C., Zawodny, N., and Pascioni, K., "Computational Study of Vortex-Induced Separation for a 5-Bladed Rotor," VFS International 79th Annual Forum & Technology Display, West Palm Beach, FL, May 2023.

26. Alba, C., Elham, A., German, B., and Veldhuis, L., "A Surrogate-Based Multi-Disciplinary Design Optimization Framework Modeling Wing–Propeller Interaction," *Aerospace Science and Technology*, Vol. 78, 2018, pp. 721–733.

27. McLemore, H., and Cannon, M., "Aerodynamic Investigation of a Four-Blade Propeller Operating through an Angle-of-Attack Range from 0 to 180 Degrees," NACA TN 3228, 1954.

28. Leng, Y., Jardin, T., Bronz, M., and Moschetta, J.-M., "Experimental Analysis of Propeller Forces and Moments at High Angle of Incidence," AIAA SciTech 2019 Forum, AIAA Paper 2019-1331, San Diego, CA, January 2019.